J Mater Sci (2006) 41:8202–8210
DOI 10.1007/s10853-006-0453-5

The degradation of novolak containing metal nitrates and the formation of YBCO

Yulia Lumelsky · Michael S. Silverstein

Received: 13 February 2006 / Accepted: 12 May 2006 / Published online: 11 November 2006

Abstract Polymers that form a complex with metal ions from nitrate salts can be used to prepare precursors for the production of high temperature superconductor (HTSC) ceramics that can be processed using advantageous polymer processing techniques and then pyrolyzed. This paper describes the production of HTSC from a precursor based on *m*-cresol formaldehyde novolak resin (*m*CFNR) that contains yttrium, barium and copper nitrate salts in the proportions needed for the formation of $YBa_2Cu_3O_{7-x}$ (YBCO). The degradation of the precursor and the effects of the pyrolysis process (temperature, time, environment, substrate) were studied in detail. The mechanisms of degradation for *m*CFNR and for the HTSC precursors were significantly different with the precursor degradation beginning at significantly lower temperatures. The optimal pyrolysis begins in an inert atmosphere to hinder $BaCO_3$ formation and then continues in oxygen to 950 °C. A dense orthorhombic YBCO film with preferential [001] orientation results from topotaxial growth on $SrTiO_3$.

Introduction

High temperature superconducting ceramics (HTSC) become superconducting at a critical temperature (T_c) above the boiling point of liquid nitrogen (77 K) [1, 2]. The HTSC-containing yttrium, barium and copper ($YBa_2Cu_3O_{7-x}$), known as YBCO, has exhibited a T_c of 91 K. A polymer solution containing dissolved metal nitrates with the metal atoms in the ratio needed for a HTSC can be used as a HTSC precursor. HTSC precursors provide a relatively simple and rapid method to produce bulk materials, free-standing thin films, micrometer-scale fibers and ribbons, and nanometer-scale fibers. HTSC precursors can be processed using advantageous polymer processing techniques such as film casting, fiber spinning and photolithography to produce complex structures that can then be pyrolyzed to HTSC. HTSC precursor processing can offer superior uniformity and better control of grain size and density as compared to processing HTSC directly from inorganic salts and oxides [3]. Recent work has shown that the pyrolysis of the HTSC precursor should first produce an amorphous metal oxide which then forms the crystalline HTSC phase [3]. Polymers that have been investigated for use in HTSC precursors include *m*-cresol formaldehyde novolak resin (*m*CFNR) [4–8], poly(methacrylic acid) [3, 5, 6, 9], polyacrylonitrile (PAN) [10, 11], poly(*N*,*N*-dicarboxymethyl)allylamine [12, 13], polyimide [14, 15], and copolymers of acrylic acid and acrylamide [16–18].

$LiNbO_3$ and $SrTiO_3$ have been used as substrates for the production of HTSC from precursor films. The results with $LiNbO_3$ have been rather inconsistent. The properties depend strongly on film thickness, reflecting the ~33% mismatch in the $LiNbO_3$/YBCO lattice constants [19]. $SrTiO_3$, with a cubic crystal structure and a lattice constant of 3.905 Å, can provide a high quality topotaxial substrate for YBCO (a = 3.82 Å, b = 3.89 Å, $c/3$ = 3.893 Å) with a lattice mismatch of ~1% [4, 20]. The high degree of anisotropy in YBCO's

Y. Lumelsky · M. S. Silverstein (✉)
Department of Materials Engineering, Technion – Israel Institute of Technology, Haifa 32000, Israel
e-mail: michaels@tx.technion.ac.il

structure and properties makes it desirable to produce highly oriented YBCO films. Topotaxial growth has yielded the best HTSC films grown to date, as determined by a multitude of metrics including critical current density (J_c), morphology, and stability over time [21]. The [001] orientation is important for the fabrication of HTSC devices and is one of the criteria for obtaining the highest J_c [22, 23].

This paper describes the pyrolysis of HTSC precursors based on *m*CFNR that contains yttrium, barium and copper nitrate salts and the formation of YBCO. *m*CFNR was chosen as the precursor polymer since it has hydroxyl groups that should be able to complex with the metal ions, since it has good film-forming properties and since it can be patterned using UV photolithography. Nitrate salts were chosen for polymer/metal complex formation since they have relatively high solubilities in the solvents for mCFNR [3, 15].

Experimental procedures

Materials

*m*CFNR was synthesized by condensation using *m*-cresol (98% pure, Aldrich), formaldehyde containing 10–15% methanol as a stabilizer (Aldrich), and sulfuric acid (98% pure, Merck). The molar ratio of *m*-cresol to formaldehyde was 1.2 and the amount of sulfuric acid catalyst was 1% of the mass of *m*-cresol. The polycondensation reaction was conducted at 90 °C under reduced pressure for 6 h with constant stirring. The resulting *m*CFNR was dissolved in acetone, precipitated in water, filtered, dried under vacuum, and then ground into a powder.

The metal nitrates were yttrium nitrate pentahydrate ($Y(NO_3)_3{\cdot}5H_2O$, Y-N, 99% pure, Aldrich), barium nitrate ($Ba(NO_3)_2$, Ba-N, 99% pure, Merck) and copper nitrate 2.5 hydrate ($Cu(NO_3)_2{\cdot}2.5H_2O$, Cu-N, 99% pure, Riedel de Haën). The solvent used for *m*CFNR was dimethylformamide (DMF, 99.8% pure, Aldrich). The substrates used were (300) lithium niobate ($LiNbO_3$) single crystal wafers (SOI Wafers) and (100) strontium titanate ($SrTiO_3$) single crystal wafers (Photox). All materials were used as received.

HTSC precursor

Previous work has shown that a 2/1 mass ratio of polymer to metal nitrates is high enough in metal nitrates to produce uniform films on pyrolysis and low enough in metal nitrates to prevent recrystallization on casting [24]. The HTSC precursor was produced by mixing a polymer solution with a solution of metal nitrates. The polymer solution was prepared by mixing *m*CFNR and DMF in a *m*CFNR/DMF mass ratio of 1/4 at 25 °C. The three metal nitrates with Y:Ba:Cu in a 1:2:3 atomic ratio ((Y,Ba,Cu)-N) were dissolved at room temperature in DMF. This solution of metal salts was then added dropwise into the polymer solution to produce the HTSC precursor. The HTSC precursor powders and films with a *m*CFNR/(Y,Ba,Cu)-N mass ratio of 2/1 will be termed henceforth '2/1'.

Precursor powders were obtained by casting a precursor solution on a Teflon plate and drying in a circulating air oven at 150 °C for 2 h and then in a vacuum oven at 25 °C for 24 h. The film was then ground using a mortar and pestle and dried in a vacuum oven at 100 °C until the weight remained constant. Precursor films were obtained by spin-casting precursor solutions on $LiNbO_3$ or $SrTiO_3$ substrates at a speed of 2,000 rpm. The resulting precursor films were dried by heating at 150 °C for 2 h in a circulating air oven.

Thermal analysis

The degradation process was characterized using differential scanning calorimetry (DSC, Mettler DSC-821 calorimeter) and thermogravimetric analysis (TGA, Setaram 92-16.18 TGA). The DSC samples were dry powders (4–6 mg) in an open pan with an empty aluminum pan as the reference. The samples were heated from 25 °C to 450 °C at 10 °C/min in flowing nitrogen (4 ml/min). The TGA samples were dry powders (20 mg). The samples were heated from 25 °C to 1,000 °C at 5 °C/min in flowing argon (30 ml/min). The differential thermal gravimetry (DTG) thermograms were derived from the TGA thermograms using the supplied software.

Structural analysis

The changes in the molecular structure on exposure to high temperatures were investigated by Fourier transform-infrared spectroscopy (FT-IR, Brucker Equinox 55 spectrophotometer). The samples were exposed to high temperatures by heating in the DSC at 10 °C/min in nitrogen. FTIR spectra from 500 cm^{-1} to 4,000 cm^{-1} at a resolution of 2 cm^{-1} were taken in transmission using KBr pellets containing 1% of the sample by weight.

The crystalline structure and the identity of the phases were determined using X-ray powder diffraction (XRD, Philips PW 1840 X-ray) with a Ni-filtered Cu-Kα X-ray beam excited at 40 kV and 40 mA. The

thicker films needed for XRD were produced by repeating the spin-casting and drying cycle five times. XRD was carried out using both a grazing angle stage ($\theta = 3°$) and a Bragg–Brentano stage (θ–2θ, in the 20°–80° 2θ range). Step scans were made with a 0.02° (2θ) step size and 12 s exposure per step.

The grain size, the grain morphology and the microstructure of the ceramic following pyrolysis were characterized using high-resolution scanning electron microscopy (HRSEM, LEO high-resolution SEM 982, Zeiss, equipped with an SE in-lens detector). The chemical composition was characterized using X-ray energy dispersive spectrometry (EDS) in the HRSEM. Quantitative elemental analysis was performed on selected areas using a matrix correction program (ZAF, LINK OPAL). The final result was normalized to 100% and averaged over a large number (at least 20) of measurements.

The crystallographic orientation was determined using electron backscattering diffraction (EBSD) in the HRSEM (LINK OPAL, Oxford Instruments, England). The Kossel pattern was generated at a working distance of 21 mm using an acceleration voltage of 20 kV and a probe diameter of about 40 nm. The bands of the Kossel pattern were automatically indexed and analyzed by the software.

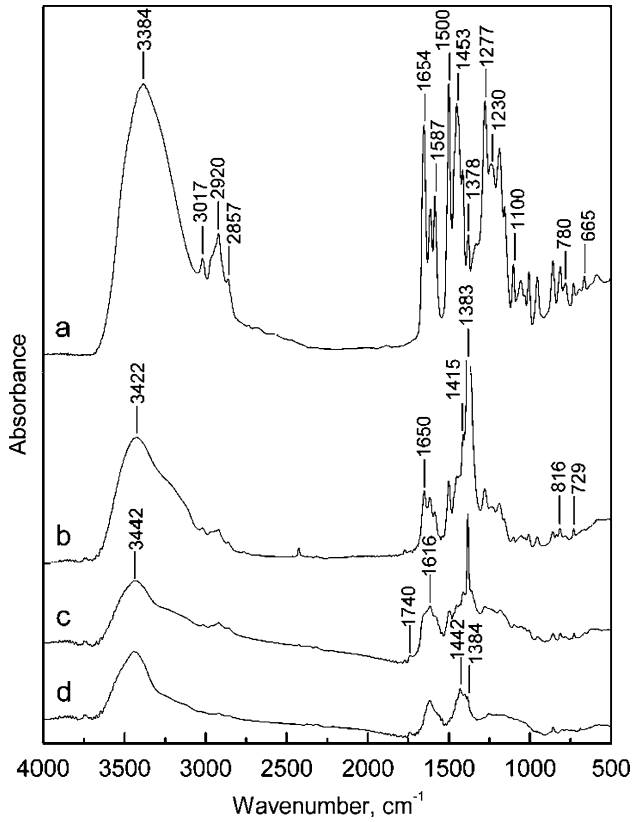

Fig. 1 FT-IR spectra of: (**a**) *m*CFNR, as-cast; (**b**) 2/1, as-cast; (**c**) 2/1, exposed to 240 °C; (**d**) 2/1, exposed to 450 °C

Results and discussion

Precursor molecular structure

The FT-IR spectrum from as-cast *m*CFNR is presented in Fig. 1a. The molecular groups associated with the major absorption bands are listed in Table 1. The *m*CFNR spectrum exhibits: a very broad and strong phenolic O–H stretching band at 3,383 cm^{-1}; *m*-cresolic CH_3 stretching, aliphatic CH_2 stretching and aromatic CH doublets bands between 2,857 cm^{-1} and 3,019 cm^{-1}; a strong ring stretching band doublet at 1,600 cm^{-1}; a weak band associated with CH_3 stretching at 1,378 cm^{-1}; a strong phenolic OH in-plane deformation band at 1,276 cm^{-1}; a group of bands associated with 3-alkyl-phenol C–OH stretching between 1,230 cm^{-1} and 1,100 cm^{-1}; medium bands from aromatic CH in-plane deformation and from out-of-plane ring deformation at 1,050 cm^{-1}. The presence of residual DMF yields bands at about 1,654 cm^{-1} and 665 cm^{-1} [25–27].

The FT-IR spectrum from as-cast 2/1 *m*CFNR/(Y,Ba,Cu)-N exhibits the typical *m*CFNR and residual DMF absorption bands described previously (Fig. 1b). In addition, the spectrum from 2/1 exhibits some bands associated with metal nitrates including: the NO_3^- asymmetric stretch from Ba-N at 1,362 cm^{-1} and the NO_3^- stretch from Y-N and Cu-N at 1,383 cm^{-1} [28, 29]. The formation of a phenoxy metallic complex is

Table 1 The FT-IR bands and their assignments

Group	Band (cm^{-1})
C=O	665
NO_3^- in-plane bend	729
Out-of plane ring deformation	780
NO_3^- out-of plane bend	816
3-alkyl-phenol C–O stretch	1,100–1,230
Phenolic OH in-plane deformation	1,277
CH_3 stretch	1,378–1,415
Cu-N and Y-N: NO_3^- asymmetric stretch	1,383
Ba-N: NO_3^- symmetric stretch	1,415
$BaCO_3$	1,442
Aliphatic CH_2 stretch	1,453
Aromatic CH stretch	1,500
Quadrant ring stretch	1,587–1,613
COO^- stretch	1,616, 1,740
Phenoxy-metal complex CO^- stretch	1,650
O=C–NH_2 (DMF)	1,654
m-cresolic CH_3 symmetric stretch	2,857
Aliphatic CH_2 asymmetric stretch	2,920
Aromatic CH stretch	3,017
Phenolic OH stretch	3,384

indicated by the presence of a band at 1,650 cm^{-1} attributed to CO^{-} stretching. This band is only found in the HTSC precursor and is not present in neat *m*CFNR or the neat nitrates [4].

The influence of the (Y,Ba,Cu)-N content on the FT-IR spectrum was determined by comparing normalized band heights. The band heights were normalized by dividing the band height by the height of the CH band at 2,857 cm^{-1}. The variation of selected normalized FT-IR band intensities with the nitrate content is seen in Fig. 2. The normalized intensity of C–OH stretching at 1,230 cm^{-1} decreases as the nitrate content increases since some of the C–OH groups are expected to complex with the metal ions. The normalized heights of the bands associated with NO_3^- and CO^-M^+ both increase with increasing nitrate content, as expected.

Precursor degradation

The DSC thermogram from as-synthesized *m*CFNR in nitrogen is presented in Fig. 3. The DSC thermogram exhibits two endothermic peaks (77 °C and 198 °C) and an exothermic peak (340 °C). The endothermic peak at 77 °C and the shoulder at about 100 °C can be associated with the evaporation of residual methanol and water, respectively. The endothermic peak at 198 °C can be associated with the evaporation of residual DMF. The small exothermic peak at 340 °C reflects the formation of a crosslinked structure [27]. The exothermic behavior above 350 °C reflects degradation of the polymer. The TGA and DTG for *m*CFNR in argon is seen in Fig. 4. *m*CFNR degrades in a series of small overlapping steps yielding a relatively continuous weight loss curve and multiple

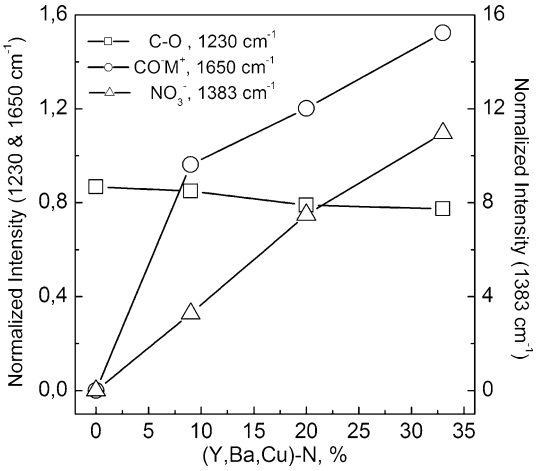

Fig. 2 Variation of as-cast normalized FT-IR band intensities with (Y, Ba, Cu)-N content

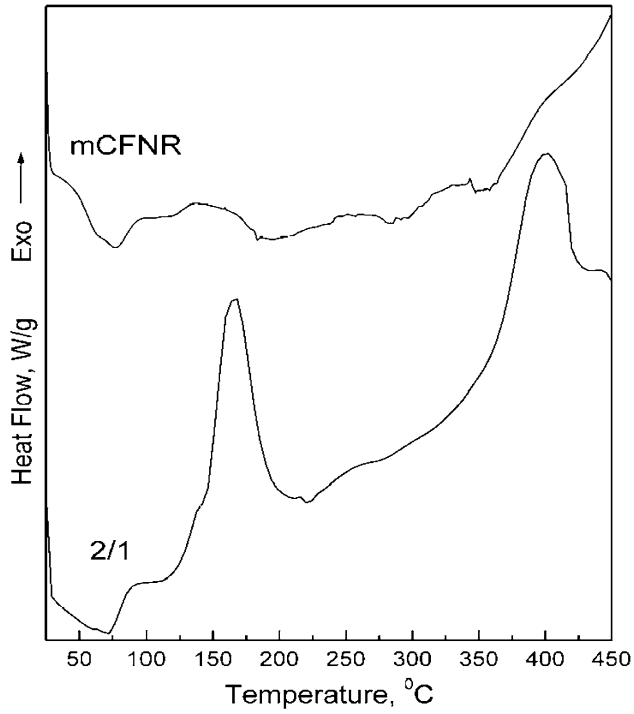

Fig. 3 DSC thermograms (5 °C/min in nitrogen) from as-received *m*CFNR and 2/1

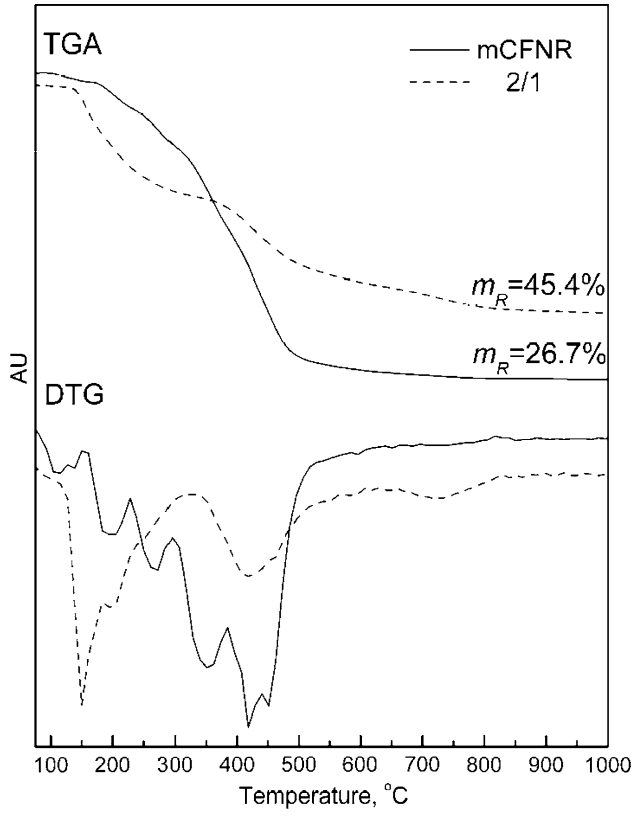

Fig. 4 TGA and DTG (10 °C/min in argon) of *m*CFNR and 2/1

DTG peaks. The DTG thermogram of *m*CFNR exhibits five peaks (Table 2). The DTG peaks at 195 °C and 350 °C correspond to the DSC peaks at 198 °C and 340 °C, respectively. The peaks at 115 °C and 195 °C are attributed to the evaporation of water and residual DMF, respectively. The DTG peaks at 273 °C, 350 °C and 452 °C correspond to the three main stages of *m*CFNR decomposition described in the literature: (1) evolution of unreacted oligomers and formation of diphenyl ether linkages from residual methylol groups; (2) formation of a crosslinked structure; (3) auto-oxidation and formation of benzophenone and carboxylic acid [26, 27, 30]. Pyrolysis of *m*CFNR in argon yields a carbonaceous residue and a residual mass, m_R, of 26.7%.

The DSC thermogram from 2/1 in nitrogen in Fig. 3 is strikingly different from the DSC thermogram from neat *m*CFNR. There are two relatively large exothermal peaks in the DSC thermogram of 2/1: the first at 170 °C and the second at 400 °C. The TGA and DTG results from the decomposition of 2/1 in argon are presented in Fig. 4 and summarized in Table 2. The initial degradation temperature is reduced from 350 °C to 150 °C on adding the metal nitrates to *m*CFNR. The degradation of 2/1 takes place in three stages, as opposed to the multiple stages seen for *m*CFNR. The first degradation stage for 2/1 is characterized by a mass loss of 26.6% that corresponds to the DSC peak at 170 °C (Table 2). The decomposition of Cu-N and Y-N takes place between 138 °C and 370 °C [10, 17, 31–36]. The oxidative degradation of the polymer is catalyzed by the presence of copper ions and nitrate ions and by the decomposition of the nitrate [10, 11, 17, 27]. The second degradation stage for 2/1, at about 400 °C, is characterized by a mass loss of 20.8% and is related to the elimination of almost all the organic matter (Table 2). The third degradation stage of 2/1 is characterized by a DTG peak at 726 °C and a mass loss of 7.2% that is associated with the decomposition of Ba-N. A constant residual mass of 45.4% was reached at 832 °C. This residual mass is greater than the residual mass of 31.7% that was calculated by assuming that the *m*CFNR produces a residual mass of 26.7% and that Y_2O_3, BaO and CuO are formed. The higher than expected residual mass may indicate that carbonates are formed during the pyrolysis of 2/1 in Ar. XRD, EDS and FT-IR will be used to confirm this conclusion (below).

Table 2 Thermal analysis of *m*CFNR and of 2/1: summary

Stage number	Onset (°C)	DTG peak (°C)	Mass loss (%)	DSC peak (°C)
*m*CFNR				
Ia	25	115	1.1	77, endo
Ib	177	195	6.1	198, endo
Ic	251	273	8.2	–
IIa	300	350	30.0	340, exo
IIb	400	418	25.2	–
III	500	596	2.7	–
Total	–	–	73.3	–
2/1				
I	25	150	26.6	170, exo
II	325	418	20.8	400, exo
III	600	726	7.2	–
Total	–	–	54.6	–

The changes in polymer molecular structure following the reactions described by the DTG peaks were determined by observing the changes in the FT-IR spectra following exposure of 2/1 to 180 °C, 240 °C or 450 °C. Following exposure of 2/1 to 180 °C (not shown), the FT-IR band at 1,650 cm^{-1} becomes more prominent and a new band 1,734 cm^{-1} appears as a shoulder on the band at 1,650 cm^{-1} [24]. These changes are related to the formation of COO^- groups and are indicative of the oxidative degradation of *m*CFNR. No such changes are observed in the FT-IR spectrum of neat *m*CFNR following exposure to 180 °C (not shown) [24]. Similar changes occur in neat *m*CFNR only following exposure to 450 °C (not shown) [24]. In 2/1, the oxidative degradation is catalyzed by the presence of copper ions and nitrate ions and occurs at significantly lower temperatures than it occurs in neat *m*CFNR.

The NO_3^- bands dominate the spectrum for as-cast 2/1, but these bands become less dominant following exposure to 240 °C (Fig. 1c). The spectrum from 2/1 following exposure to 450 °C (Fig. 1d) still exhibits a small absorption at 1,384 cm^{-1}. The nitrate ion from the more thermally stable Ba-N is still present at this temperature. The appearance of a band at 1,442 cm^{-1} in 2/1 following exposure to 450 °C most likely indicates the formation of carbonate groups, as will be confirmed through XRD and EDS (below) [4, 12, 13].

Formation of YBCO

The 'S1' pyrolysis process was used to synthesize YBCO powders from 2/1. The 'S1' process includes: (1) pyrolysis from 25 °C to 450 °C at 5 °C/min and holding at 450 °C for 2 h, heating to 950 °C at 5 °C/min (all in nitrogen); (2) sintering in air at 950 °C for 1 h. The first step was used to prevent the formation of metal oxides and $BaCO_3$ and the second step was used to completely decompose the organic compounds and to provide the oxygen needed for the formation of $YBa_2Cu_3O_{7-x}$. The powder from the "S1" process

was characterized using XRD. All the reflections in Fig. 5a corresponded to highly pure, randomly oriented, orthorhombic $YBa_2Cu_3O_{7-x}$. The resulting YBCO nano-crystals, about 90 nm in thickness and 500 nm in length, are seen in the HRSEM micrographs in Fig. 6.

The pyrolysis of 2/1 films on $LiNbO_3$ using the "S1" process yielded poor results, individual grains of YBCO distributed among other phases ($Cu_2Y_2O_5$, $BaCuO_2$ and Y_2O_3, not shown) [24]. Although the "S1" process was successful in producing YBCO powder from the precursor powder, it was not successful in producing YBCO films from precursor films. The differences between the pyrolyzed powder and film may reflect the greater surface area in the powder which would promote the formation of YBCO by enhancing the diffusion of oxygen inwards and pyrolysis products outwards. In order to enhance YBCO formation in films, the pyrolysis process was modified by increasing the annealing time for enhanced diffusion. An additional difference between the pyrolysis of powders and films is the presence of a substrate. The

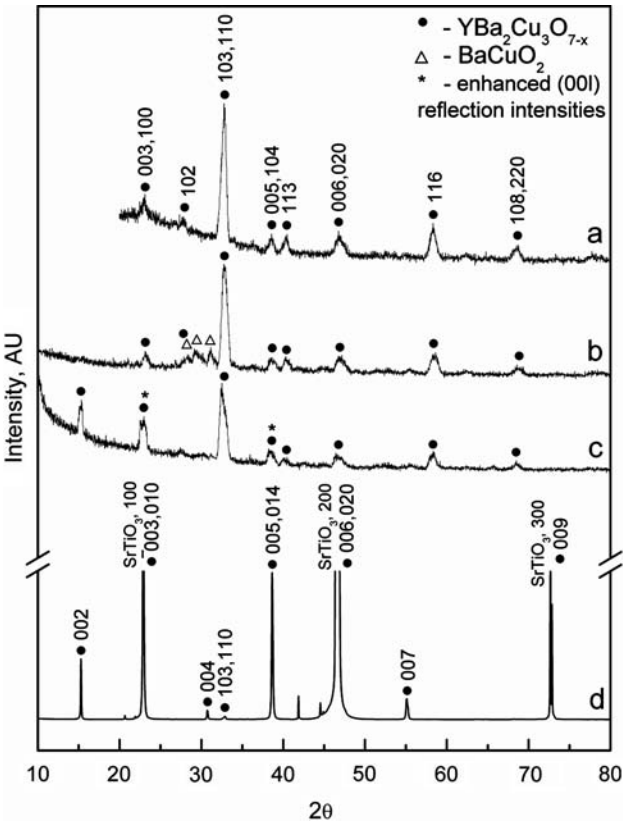

Fig. 5 XRD spectra of 2/1 following pyrolysis using: (**a**) 'S1' for a powder; (**b**) 'S2a' for a cast film on $SrTiO_3$; (**c**) 'S2b' for a cast film on $SrTiO_3$, grazing angle (θ=3°); (d) 'S2b' for a cast film on $SrTiO_3$, Bragg–Brentano geometry (θ–2θ)

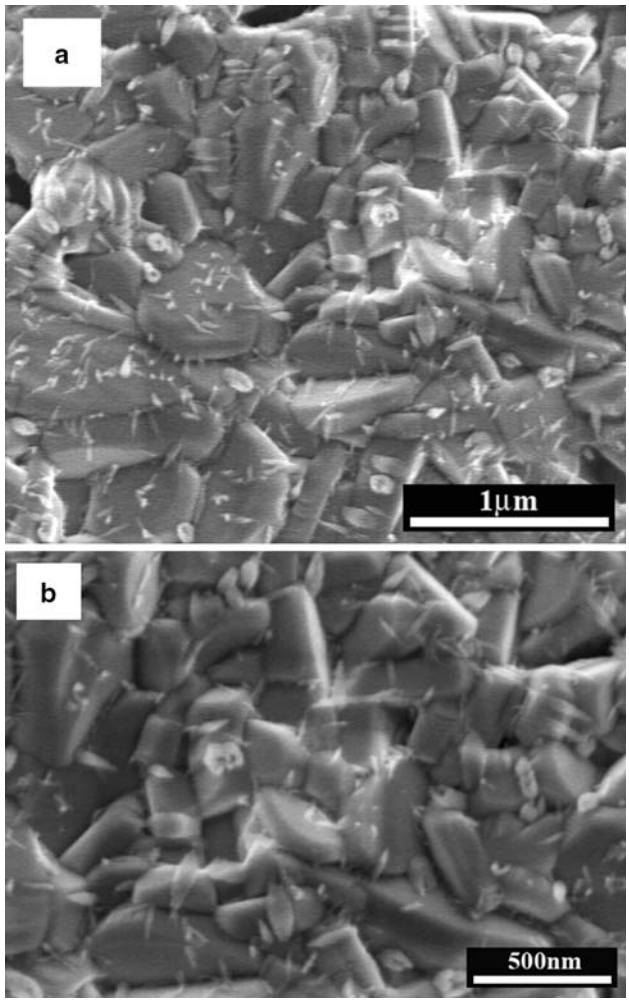

Fig. 6 HRSEM micrographs of a powder prepared from a 2/1 powder using the 'S1' process. (**a**) Lower magnification and (**b**) Higher magnification

substrate can exert considerable influence on the microstructure of the film through: a reaction with the film; a coefficient of thermal expansion mismatch; a lattice parameter mismatch; the surface roughness, homogeneity and cleanliness [21, 37, 38].

Pyrolysis processes 'S2a' and 'S2b' include: (1) heating from 25 °C to 450 °C at 5 °C/min, holding at 450 °C for 2 h, heating to 700 °C at 5 °C/min (all in nitrogen); (2) heating to 950 °C at 10 °C/min, holding at 950 °C (for either 1.5 h ('S2a') or 3 h ('S2b')), cooling to 450 °C at 3 °C/min, holding at 450 °C for 3 h, cooling to room temperature at 3 °C/min (all in oxygen). Process 'S2a' for 2/1 on $LiNbO_3$ yielded a randomly oriented, porous $YBa_2Cu_3O_{7-x}$ film that contained some contaminant phases ($BaCuO_2$ and $Cu_2Y_2O_5$, not shown) [24]. These results were a substantial improvement over 'S1' with respect to the yield of YBCO. The yield of YBCO was enhanced

even further by using the 'S2a' process for 2/1 on $SrTiO_3$. 'S2a' for 2/1 on $SrTiO_3$ (Fig. 5b) produced a randomly oriented $YBa_2Cu_3O_{7-x}$ film with a relatively small $BaCuO_2$ contaminant content. The reduction in the concentration of contaminant phases on using $SrTiO_3$ demonstrates the importance of the substrate for the nucleation and growth of particular phases. 'S2a' on $SrTiO_3$ yields YBCO that consists of densely packed small grains of about 250 nm in size (Fig. 7).

The YBCO film on $SrTiO_3$ from 2/1 using the 'S2b' process (Fig. 8a) consists of spherical grains that are extensively interconnected. It is difficult to gauge the actual grain size from the HRSEM micrographs owing to the extensive grain intergrowth. A spiral grain growth mechanism is clearly visible in Fig. 8b. The grain size has increased markedly with the increase in time at 950 °C. These changes are similar to the grain growth in thermodynamically controlled recrystallization [3]. The atomic compositions of several grains seen in Fig. 8 were determined using EDS in the HRSEM. The grains exhibit a Y:Ba:Cu:O ratio of 0.9:2.0:3.0:6.9

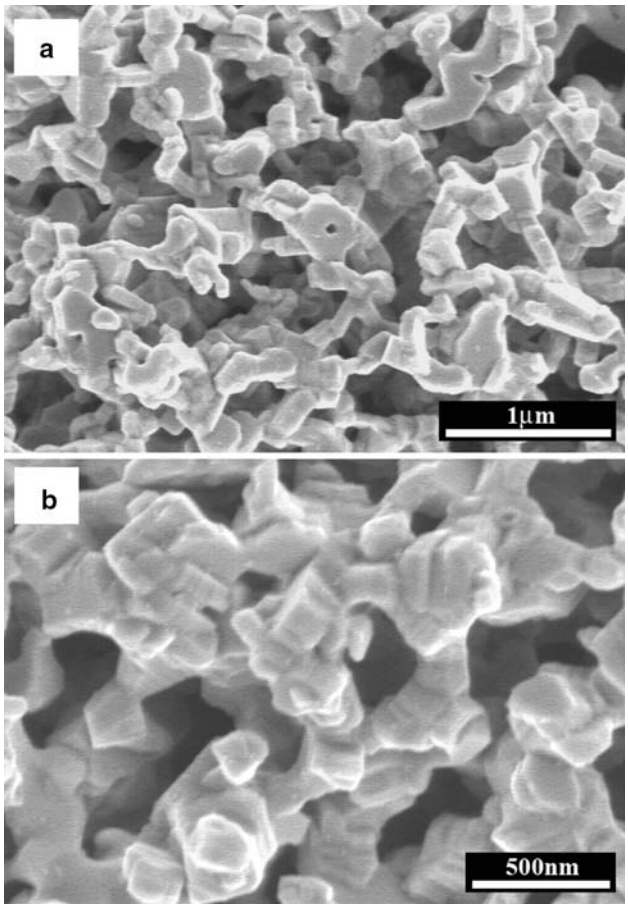

Fig. 7 HRSEM micrographs of a film prepared from 2/1 on $SrTiO_3$ using the 'S2a' process. (**a**) Lower magnification and (b) Higher magnification

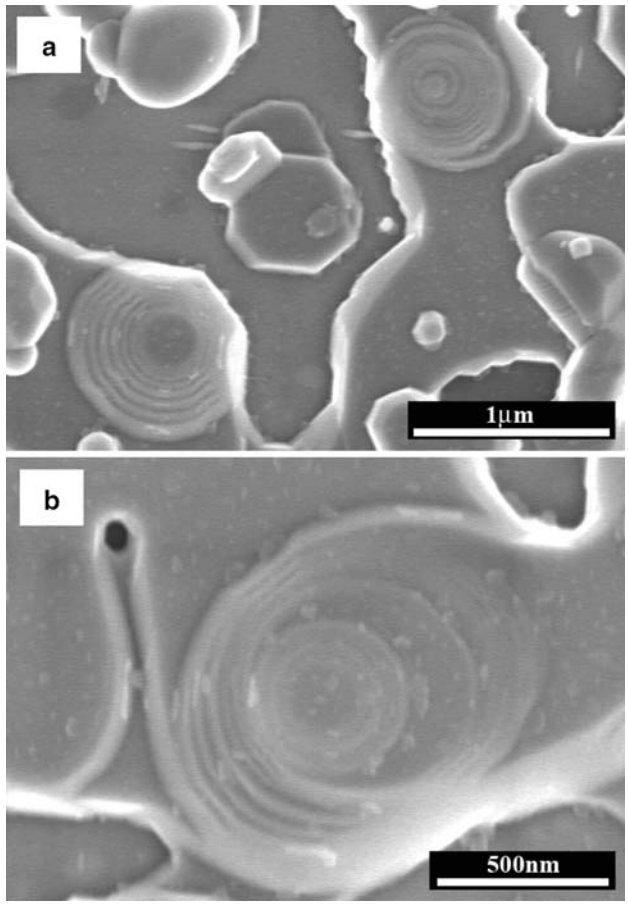

Fig. 8 HRSEM micrographs of a film prepared from 2/1 on $SrTiO_3$ using the 'S2b' process. (**a**) Lower magnification and (**b**) Higher magnification

(Table 3). The differences between the measured atomic composition and the expected atomic composition are within the experimental error of the technique.

The 'S2b' process on $SrTiO_3$ yields only orthorhombic YBCO (Fig. 5c). The essential difference between 'S2a' and 'S2b' is the extra sintering time in oxygen at 950 °C which yields the dense YBCO in Fig. 8. The intensities of the (003) and (005) reflections in Fig. 5c (marked with asterisks) are more predominant than those seen from the randomly oriented materials in Fig. 5a,b and are more predominant than those from a YBCO powder in the literature [39]. The relatively

Table 3 EDS from a 2/1 film on $SrTiO_3$ pyrolyzed using the 'S2b' process

	Y (at%)	Ba (at%)	Cu (at%)	O (at%)	Y:Ba:Cu:O
Calculated	7.7	15.4	23.1	53.8	1:2:3:6.8
Measured	7.2±0.5	15.7±1.9	23.2±1.3	53.9±3.8	0.9:2:3:6.9

high intensities of the (003) and (005) peaks indicate that the 'S2b' process for 2/1 on $SrTiO_3$ has produced an oriented YBCO structure.

The formation of oriented YBCO from 2/1 on $SrTiO_3$ using the 'S2b' process was confirmed using X-ray diffraction with a Bragg–Brentano geometry θ–2θ (Fig. 5d). Most of the strong intensities in the Bragg–Brentano (θ–2θ) X-ray spectrum (Fig. 5d) belong to the set of (001) reflections with l in (h k l) ranging from 1 to 9. In addition, there are the (013) and (103)/(110) doublet reflections at 2θ of 32.5° and 32.8°, respectively. The relative heights of the (100) and (200) reflections are much smaller than those found in the JCPDS data for randomly ordered powder, again emphasizing the high degree of orientation in the film. The predominance of the (001) reflections indicates that the c-axis of the orthorhombic YBCO is orientated preferentially perpendicular to the substrate surface. This orientation is consistent with the spiral grain growth morphology seen in the HRSEM micrographs (Fig. 8). The step height on the spiral corresponds to the unit cell (c-axis) of crystalline YBCO. The intensity ratio I(005)/I(103,110) is called the 'orientation index' (OI) and is used to estimate the degree of orientation [15]. The YBCO film in Fig. 5d has an OI of 18.8, while a powder, having a completely random orientation, has an OI of 0.11 (from the JCPDS data) [39].

The high degree of orientation in this film was also confirmed by EBSD. EBSD analysis of thin films produces crystallographic information that is difficult to acquire by other techniques. The Kikuchi-like Kossel pattern generated by the EBSD of an HTSC film from 2/1 on $SrTiO_3$ using the 'S2b' process is seen in Fig. 9a. The set of indices from orthorhombic YBCO that overlays the experimental pattern in Fig. 9b indicates that [001] is the dominant direction, confirming that the YBCO is highly oriented, with the c-axis perpendicular to the substrate. The highly oriented YBCO suggests that there has been topotaxial growth from the $SrTiO_3$.

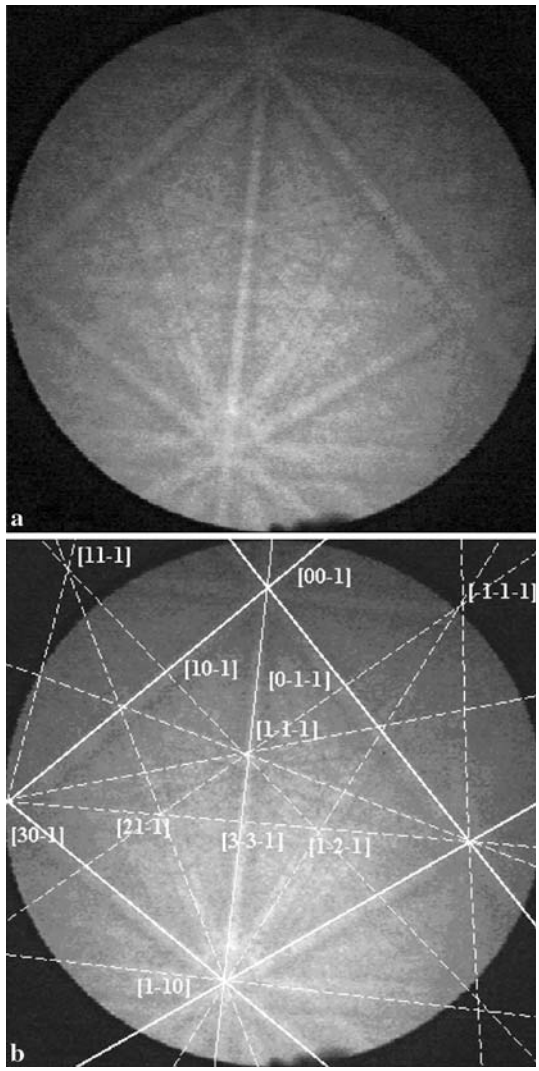

Fig. 9 EBSD from a film prepared from 2/1 on $SrTiO_3$ using the 'S2b' process: (**a**) The measured patterns and (b) The measured patterns with indexing of the planes

Conclusions

The thermal degradation of an HTSC precursor based on *m*CFNR and the results of precursor pyrolysis were investigated. Polymer–metal ion complexes were formed in the precursor film. There were significant differences between the thermal degradation of *m*CFNR and the thermal degradation of the precursor. The thermal degradation of the precursor in argon, catalyzed by the presence of copper ions and nitrate ions, began at a relatively low temperature and occurred in three distinct stages. The relatively high residual mass of 45.4% from the degradation of the precursor in argon indicates that carbonates were formed. YBCO formation was appreciably affected by the pyrolysis process (temperature, time, environment, substrate). Pyrolysis of the precursor powder, beginning in nitrogen and continuing in air, yielded a highly pure, orthorhombic YBCO powder. This process, however, did not produce high quality YBCO films. Pyrolysis of the precursor on $SrTiO_3$ at 950 °C in oxygen for longer times produced a highly oriented, high purity, orthorhombic YBCO film with a [001] c-axis orientation perpendicular to the substrate surface from topotaxial growth and with no detectable contaminant phases.

Acknowledgements The authors gratefully acknowledge the partial support of the German-Israeli Foundation and the Technion VPR Fund. The authors gratefully acknowledge A. Siegmann, W. D. Kaplan, G. Shter, G. Grader and I. von Lampe with thanks for their most helpful discussions.

References

1. Bednorz G, Müller KA (1986) Z Phys B64:189
2. Wu MK, Ashborn JR, Torng CJ, Hor PH, Meng RL, Gao L, Huang ZJ, Wang YQ, Chu CW (1987) Phys Rev Lett 58:908
3. Chien JCW, Gong BM, Madsen JM, Halock RM (1988) Phys Rev B 38:11853
4. von Lampe I, Schultze D, Zygalsky F, Silverstein MS (2003) Polym Degrad Stabil 81:57
5. von Lampe I, Schmalstieg A, Götze S, Muller JP, Zygalsky F, Lorkowski HJ, Matalla M (1997) J Mater Sci Lett 16:16
6. von Lampe I, Bruckner A, Götze S (1997) Die Angew Makromol Chem 251:157
7. von Lampe I, Götze S, Zygalsky F (1996) J Low Temp Phys 105:1289
8. von Lampe I, Waesche M, Krueger RP, Lorkowski HJ (1994) Fresenius' J Anal Chem 349:256
9. von Lampe I, Schultze D, Zygalsky F (2001) Polym Degrad Stabil 73:87
10. Silverstein MS, Najary Y, Grader GS, Shter GE (2001) J Polym Sci Part B: Polym Phys 42:1023
11. Silverstein MS, Najary Y, Lumelsky Y, von Lampe I, Grader GS, Shter GE (2004) Polymer 45:937
12. Naka K, Hagihara K, Tanaka Y, Tachiyama Y, Ohki A, Maeda S (1996) J Mater Sci 31:6389
13. Naka K, Tachiyama Y, Ohki A, Maeda S (1996) J Polym Sci: Part A: Polym Chem 34:1003
14. Maeda S, Tsurusaki Y, Tachiyama Y, Naka K, Ohki A, Ohgushi T, Takeshita T (1994) J Polym Sci: Part A: Polym Chem 32:1729
15. Chien JCW, Gong BM, Mu X, Yang YS (1990) J Polym Sci: Part A: Polym Chem 28:1999
16. Pomogailo AD, Savost'ynov VS, Dzardimalieva GI, Dubovitskii AV, Ponomaryev AN (1995) Izv Akad Nauk Ser Khim 6:1096
17. Dubinsky S, Grader GS, Shter GE, Silverstein MS (2004) Polym Degrad Stabil 86:171
18. Dubinsky S, Lumelsky Y, Grader GS, Shter GE, Silverstein MS (2005) J Polym Sci: Part B: Polym Phys 43:1168
19. Hoehler A, Guggi D, Neeb H (1989) Appl Phys Lett 54:1066
20. Naka K, Tanaka Y, Yamasaki K, Ohki A, Chujo Y, Maeda S (2001) Bull Chem Soc Jpn 74:571
21. Phillips JM (1996) J Appl Phys 79:1829
22. Chaudhari P, Koch RH, Laibowitz RB, McGuire TR, Gambino RJ (1987) Phys Rev Lett 58:2684
23. Yee DS, Gambino RJ, Chisholm MF, Cuomo JJ, Madakson P, Karasinski J (1988) AIP Confer Proc 165:132
24. Lumelsky Y (2004) M.Sc. Thesis, Department of Materials Engineering, Technion, Haifa, Israel
25. Hummel DO (1998) Atlas of polymer and plastics analysis 2 Part b/I. Carl Hanser Verlag, Munich, pp 428–433
26. Costa L, Rossi di Monterela L, Gamino G, Weil ED, Pearce EM (1997) Polym Degrad Stabil 56:23
27. von Lampe I, Kunze R, Neubert D, Günther W (1995) Polym Degrad Stabil 50:337
28. Colthup NB, Daly LH (1990) Introduction to infrared and Raman spectroscopy, 3rd edn. Academic Press, New York
29. Rojas RM, Kovacheva D, Petrov K (1999) Chem Mater 11:3263
30. Jackson WM, Conley RT (1964) J Appl Polym Sci 8:2163
31. Cseri T, Bekassy S, Kenessy G, Liptay G, Figueras F (1996) Thermochim Acta 288:137
32. Taylor TJ, Dollimore D, Gamlen GA (1986) Thermochim Acta 103:333
33. Zivkovic ZD, Zivkovic DT, Grujicic DB (1998) J Therm Anal Calorim 53:617
34. Hamdy MI, Hussein Gamal AM (1996) Powder Technol 87:87
35. Hussein Gamal AM (1994) Thermochim Acta 244:139
36. Jergel M, Chromik S, Strbik V, Smatko V, Hanic F, Plesch G, Buchta S, Valtyniova S (1992) Supercond Sci Technol 5:225
37. Cyrot M, Pavuna D (1992) Introduction to superconductivity and high-Tc materials. World Scientific, Singapore, pp 212–213
38. Singh RK, Kumar D (1998) Mater Sci Eng: R: Rep 22:113
39. Joint Committee on Powder Diffraction Studies (JCPDS) Card 39-0486